SCIENCE CHINA
Information Sciences

• RESEARCH PAPER •

Fully actuated system approach for quantum spin dynamics: modeling and decoupling control

Zhuo Wang[1], Jiahang Li[1], Ruigang Wang[2*], Feng Li[1,3], Shan Xue[4], Yong Xu[5] & Qinglai Wei[6]

[1]*School of Instrumentation and Optoelectronics Engineering, Beihang University, Beijing* 100191, *China*
[2]*School of Information Science and Technology, Hangzhou Normal University, Hangzhou* 311121, *China*
[3]*Hangzhou Innovation Institute, Beihang University, Hangzhou* 310051, *China*
[4]*School of Information and Communication Engineering, Hainan University, Haikou* 570228, *China*
[5]*Guangdong Provincial Key Laboratory of Intelligent Decision and Cooperative Control, School of Automation, Guangdong University of Technology, Guangzhou* 510006, *China*
[6]*State Key Laboratory for Management and Control of Complex Systems, Institute of Automation, Chinese Academy of Sciences, Beijing* 100190, *China*

Abstract Independent manipulation of atomic spin polarization in spin-exchange relaxation-free (SERF) magnetometer is fundamentally hindered by the inherent nonlinearity and singularity of the Bloch equation, which renders the system a first-order sub-fully actuated system (sub-FAS) under standard magnetic control. To address this challenge, a high order fully actuated system (HOFA) approach is developed to reconstruct the actuation structure by introducing pump laser intensity as an additional physical input. The augmented model becomes a redundant fully actuated system on an admissible domain where the input matrix achieves full row rank, and a HOFA representation is derived by treating the input rate as a virtual control. An explicit analytic controller is obtained via exact cancellation and parametric eigenstructure assignment, together with a right-inverse allocation that resolves redundancy while preserving the desired linear error dynamics. This approach theoretically achieves complete dynamic decoupling of the strongly coupled quantum spin states, transforming the complex nonlinear quantum control problem into a linear constant one. Simulation results validate that the proposed method significantly outperforms traditional strategies in decoupling accuracy and tracking performance.

Keywords fully actuated system, quantum spin dynamics, atomic sensors, SERF magnetometer, dynamic decoupling

Citation Fully actuated system approach for quantum spin dynamics: modeling and decoupling control. Sci China Inf Sci, for review

1 Introduction

Quantum spin dynamics under optical pumping and magnetic actuation form the physical core of a broad class of quantum precision sensors [1–4]. Spin-exchange relaxation-free (SERF) magnetometers are representative systems that achieve ultra high sensitivity in weak magnetic field detection [5, 6]. The ensemble averaged spin polarization obeys Bloch dynamics, and high performance magnetometry requires accurate and broadband manipulation of the polarization state [7, 8]. From the control theoretic perspective, this task remains challenging because the magnetic actuation enters through a vector cross product, which produces a strongly nonlinear, state dependent, and intrinsically coupled input mapping. Conventional controller designs often aim to suppress cross-axis coupling through local linearization and disturbance rejection [9–12]. Such approaches can be effective near an operating point but do not provide a synthesis mechanism that guarantees wide range regulation and dynamic decoupling, which constrains the achievable bandwidth and dynamic range.

To improve the dynamic performance of atomic sensors, a variety of control strategies have been explored. PID control and its variants remain widely adopted in engineering practice due to their simplicity, yet linear feedback can suffer from reduced stability margins when the system operates far from the nominal point under large disturbances and strong coupling [13]. Model-based techniques have been introduced to mitigate parameter uncertainties and external noise, and data driven components have been incorporated to estimate and compensate coupling effects [14, 15]. Despite these advances, a common limitation is that the cross-product nonlinearity is frequently handled as an adverse perturbation rather than being treated as a structural feature that can be exploited for controller synthesis. Consequently, closed loop performance often remains tied to local approximation accuracy and tuning heuristics, and provable decoupling over a wide operating domain is difficult to obtain.

* Corresponding author (email: ruigangwang@hznu.edu.cn)

ACCEPTED

https://www.sciengine.com/doi/10.1007/s11432-026-4965-x

Recent theoretical studies further indicate that the structural limitation is not merely a matter of tuning. Controllability [16] and reachability [17] analysis for SERF spin polarization under standard single beam operation shows that the state is not completely reachable when only tri-axial magnetic fields are used as active inputs. This result reveals a fundamental mismatch between the conventional actuation configuration and the objective of independent three-axis state regulation. It also highlights a key principle in control design, namely that achievable performance is determined by the structural properties exposed by the chosen model.

The fully actuated system (FAS) approach [18] provides a synthesis-oriented framework that directly emphasizes actuation structure. The approach generalizes the concept of full actuation and enables exact cancellation and parametric assignment by constructing a model form in which control authority is explicitly characterized [19–21]. When full actuation holds, the nonlinear dynamics can be transformed into a linear closed loop system with constant parameters through an analytic feedback design, which naturally supports decoupling by eigenstructure assignment [22–24]. The FAS approach has been widely applied to rigid body attitude control, spacecraft rendezvous, and underactuated mechanical systems [25–32]. However, quantum spin dynamics governed by Bloch equations exhibit a distinctive algebraic singularity under standard magnetic actuation. The magnetic input mapping is skew symmetric and rank deficient for nonzero spin polarization, which implies that instantaneous control authority is restricted to the subspace orthogonal to the spin vector. This rank deficiency corresponds to a sub-FAS and prevents independent three-axis regulation within the conventional magnetic only configuration [33].

A FAS viewpoint therefore motivates a modeling reconstruction rather than a purely compensatory design. The central idea is to augment actuation so that the reconstructed model satisfies a full actuation condition and admits an analytic decoupling controller. Pump laser intensity provides a physically meaningful additional channel because it directly shapes the longitudinal polarization through optical pumping and introduces an actuation direction that is not confined to the orthogonal complement of the spin vector. By incorporating pump intensity as an active fourth input, the original rank-deficient structure is transformed into a FAS with redundant inputs. This redundancy is not a complication but a resource that enables control allocation to realize a desired virtual command.

The contributions are summarized as follows. First, a FAS perspective is established for quantum spin dynamics and provides a synthesis oriented interpretation of the algebraic singularity in Bloch model. Second, a high order fully actuated (HOFA) model is developed for SERF magnetometers by incorporating pump laser intensity control input, which resolves the structural rank deficiency of standard magnetic actuation. Third, an explicit decoupling controller with analytic allocation is derived to achieve exact cancellation and parametric eigenstructure assignment, thereby providing a rigorous foundation for wide-range tracking and three-axis dynamic decoupling in SERF magnetometers.

The remainder of this paper is organized as follows. Section 2 formulates the SERF spin polarization dynamics and clarifies the structural singularity that limits magnetic only regulation. Section 3 reviews the FAS framework and the parametric assignment tools that underpin the subsequent controller synthesis. Section 4 constructs a fully actuated model for the SERF system by incorporating pump laser actuation and derives a high order fully actuated representation suitable for decoupling design. Section 5 presents an explicit FAS controller together with an analytic control allocation law and establishes closed loop stability and decoupling properties. Section 6 reports numerical simulations that validate wide-range tracking, dynamic decoupling, and disturbance rejection. Section 7 concludes the paper.

2 Problem formulation

The system under investigation is a SERF atomic magnetometer, typically composed of an alkali metal vapor cell, optical pump and probe lasers, and electromagnetic coils. The vapor cell is heated to a high temperature to maintain a high atomic density. A circularly polarized pump laser propagating along the z-axis is employed to polarize the atomic spins. The optical pumping process transfers angular momentum from photons to atoms and creates a macroscopic spin polarization. To sustain the SERF regime, triaxial electromagnetic coils generate a compensation magnetic field to maintain the system operation in a near zero magnetic field environment, where the rate of spin exchange collisions far exceeds the Larmor precession frequency. In this regime, the spin exchange relaxation is effectively suppressed, allowing for ultra high sensitivity. The schematic diagram of the system is illustrated in Figure 1.

The dynamical behavior of the ensemble-averaged electron spin polarization vector is denoted by the state vector $\boldsymbol{P}(t) = [P_x(t)\ P_y(t)\ P_z(t)]^\top \in \mathbb{R}^3$ and is governed by the Bloch equation. Considering the interactions involving the magnetic field, the optical pumping, and the relaxation processes, the time evolution of the spin polarization is

https://www.sciengine.com/doi/10.1007/s11432-026-4965-x

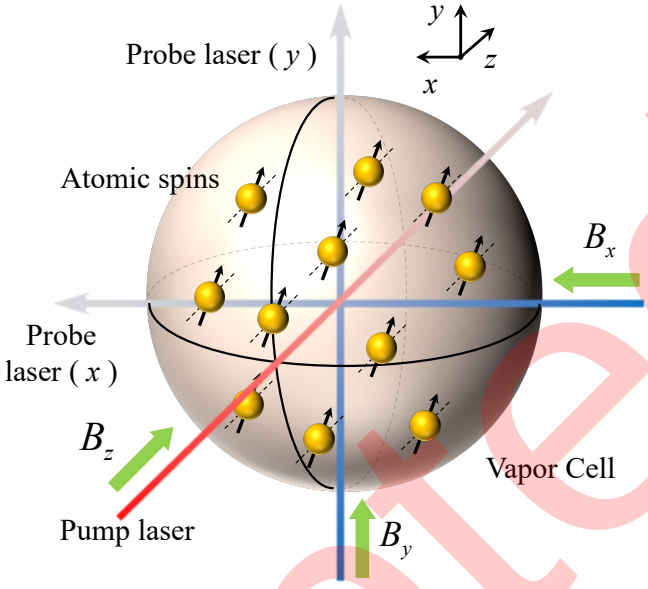


Figure 1 Schematic of SERF atomic spin principle.

described by

$$\dot{\boldsymbol{P}}(t) = \frac{1}{q}\left[\gamma_e \boldsymbol{P}(t) \times \boldsymbol{B}(t) + R_p(t)\big(\boldsymbol{S}_p - \boldsymbol{P}(t)\big) - R_{\text{rel}}\, \boldsymbol{P}(t)\right], \tag{1}$$

where the parameters are defined as follows:

γ_e is the electron gyromagnetic ratio, which determines the coupling strength between the spin polarization and the magnetic field.

q is the nuclear slowing down factor, which accounts for the effective reduction of the electron spin precession rate due to hyperfine coupling in the SERF regime.

R_{rel} is the spin relaxation rate, which is primarily determined by spin destruction collisions and wall collisions.

$\boldsymbol{S}_p$ is the photon spin vector of the pump laser. The pump beam is aligned with the z-axis and thus $\boldsymbol{S}_p = [0\ 0\ 1]^\top$.

$R_p(t)$ is the optical pumping rate, which is proportional to the pump laser intensity.

$\boldsymbol{B}(t) = [B_x(t)\ B_y(t)\ B_z(t)]^\top$ is the total magnetic field experienced by the atoms.

Equation (1) describes a nonlinear dynamical system due to the cross-product term $\boldsymbol{P}(t)\times\boldsymbol{B}(t)$. This term couples the evolution of the three spin components and makes precise manipulation of the polarization state challenging. From a control perspective, the cross product interaction imposes a geometric constraint in the sense that the magnetic torque is always orthogonal to the instantaneous spin vector. Consequently, the control input mapping associated with the magnetic field is skew symmetric and rank deficient for all $\boldsymbol{P}(t) \neq \boldsymbol{0}$. This structural singularity implies that the system lacks instantaneous control authority along the direction of $\boldsymbol{P}(t)$ and therefore cannot independently regulate the three spin components using magnetic fields alone.

Furthermore, traditional control strategies often rely on local linearization around an operating point, which is typically chosen near the zero field condition. Such approximations are suitable for small signal regulation but do not capture the wide range nonlinear dynamics required for large angle spin precession and fast trajectory tracking. The strong coupling and the state dependent control effectiveness motivate a modeling approach that explicitly addresses both the nonlinearity and the structural singularity of the Bloch dynamics.

3 Preliminaries

This section reviews the High Order Fully Actuated System (HOFA) framework that will be used for controller synthesis in subsequent sections. We present the canonical HOFA representation, the full actuation criterion, and a parametric feedback design that yields a constant closed loop linear dynamics.

Accepted

https://www.sciengine.com/doi/10.1007/s11432-026-4965-x

3.1 Notations

For a vector $x \in \mathbb{R}^r$ and an integer $k \geqslant 0$, define the stacked derivative vector [19]

$$x^{(0\sim k)} = \left[x^\top \ \dot{x}^\top \ \cdots \ x^{(k)\top}\right]^\top \in \mathbb{R}^{(k+1)r}. \tag{2}$$

For matrices $A_i \in \mathbb{R}^{r\times r}$ with $i = 0, 1, \ldots, n-1$, define

$$A_{0\sim n-1} = \left[A_0 \ A_1 \ \cdots \ A_{n-1}\right]. \tag{3}$$

Define the companion-like block matrix $\Phi(\cdot)$ and the canonical input matrix B_c as

$$\Phi(A_{0\sim n-1}) = \begin{bmatrix} 0 & I_r & & 0 \\ & 0 & I_r & \\ & & \ddots & \ddots \\ 0 & & & I_r \\ -A_0 & -A_1 & \cdots & -A_{n-1} \end{bmatrix}, \quad B_c = \begin{bmatrix} 0 \\ \vdots \\ 0 \\ I_r \end{bmatrix}. \tag{4}$$

3.2 HOFA representation and full actuation

The HOFA framework describes a class of high order nonlinear systems in a canonical input affine form.

Definition 1 ([18]). A nonlinear system admits an nth order HOFA representation if there exists a vector $x \in \mathbb{R}^r$ such that its dynamics can be written as

$$x^{(n)} = f\left(x^{(0\sim n-1)}, t\right) + B\left(x^{(0\sim n-1)}, t\right) u, \tag{5}$$

where $u \in \mathbb{R}^r$ is the control input, $f(\cdot) \in \mathbb{R}^r$ is the drift term, and $B(\cdot) \in \mathbb{R}^{r\times r}$ is the input matrix.

Definition 2 ([18]). The system (5) is called a high order fully actuated system if

$$\det B\left(x^{(0\sim n-1)}, t\right) \neq 0, \tag{6}$$

holds for all $x^{(0\sim n-1)}$ and all t in the operating domain.

Condition (6) ensures that the control channel is invertible, which enables exact cancellation of the nonlinear drift and allows the closed loop dynamics to be assigned through parametric design.

3.3 Parametric feedback design

A key consequence of the HOFA representation is that, under full actuation, a static state feedback can transform the nonlinear system into a constant linear differential equation with designer specified coefficients.

Lemma 1 ([21]). Consider the system (5) under the full actuation condition (6). Let $A_i \in \mathbb{R}^{r\times r}$ for $i = 0, \ldots, n-1$ be constant design matrices such that the matrix polynomial

$$D(\lambda) = I_r\lambda^n + A_{n-1}\lambda^{n-1} + \cdots + A_0, \tag{7}$$

is Hurwitz. Then the feedback law

$$u = -B^{-1}\left(x^{(0\sim n-1)}, t\right)\left[f\left(x^{(0\sim n-1)}, t\right) + \sum_{i=0}^{n-1} A_i x^{(i)}\right], \tag{8}$$

yields the closed loop dynamics

$$x^{(n)} + \sum_{i=0}^{n-1} A_i x^{(i)} = 0. \tag{9}$$

To incorporate trajectory tracking, the HOFA-based linear dynamics (9) can be combined with integral action to remove steady-state errors under constant disturbances.

Lemma 2 ([21]). Let $y_c(t) \in \mathbb{R}^r$ be a reference trajectory and define the tracking error $e(t) = x(t) - y_c(t)$. Introduce an integral state $z(t)$ defined by $\dot{z}(t) = e(t)$. If the augmented closed loop dynamics formed by (9) and $\dot{z}(t) = e(t)$ are Hurwitz under the selected design parameters, then the tracking error satisfies $\lim_{t\to\infty} e(t) = 0$ for constant disturbances entering additively in the $x^{(n)}$ channel.

Accepted

https://www.sciengine.com/doi/10.1007/s11432-026-4965-x

4 HOFA modeling of the SERF system

This section develops a second-order HOFA model for the SERF spin polarization dynamics by exploiting the multiphysics actuation of tri-axial magnetic fields and the pump laser intensity channel. The resulting model provides the basis for the subsequent controller synthesis under full actuation.

4.1 Control-affine SERF model

Following the SERF model in Section 2, define the state as the three dimensional electron spin polarization

$$\boldsymbol{P} = \begin{bmatrix} P_x & P_y & P_z \end{bmatrix}^\top \in \mathbb{R}^3, \tag{10}$$

and define the multiphysics control input as

$$\boldsymbol{u} = \begin{bmatrix} \boldsymbol{u}_m^\top & u_l \end{bmatrix}^\top = \begin{bmatrix} B_x & B_y & B_z & u_l \end{bmatrix}^\top \in \mathbb{R}^4, \tag{11}$$

where $\boldsymbol{u}_m = [B_x \ B_y \ B_z]^\top$ denotes the commanded magnetic fields generated by the coils and u_l denotes the pump laser actuation channel that is proportional to the optical pumping rate.

Remark 1. The control variable u_l represents the controllable component of the optical pumping rate $R_p(t)$. In a practical SERF magnetometer, R_p is proportional to the pump laser intensity and the alkali-metal absorption cross section: $R_p = \Phi \cdot \sigma(\nu)$, where Φ is the photon flux proportional to the pump laser intensity I_{pump} and $\sigma(\nu)$ is the absorption cross section at the laser frequency ν. Modulation of u_l can be realized by: (i) directly modulating the pump laser diode current, which provides bandwidth up to several hundred kHz; or (ii) using an acousto-optic modulator (AOM) or electro-optic modulator (EOM) in the beam path, offering modulation bandwidth exceeding 1 MHz. Both approaches are standard in atomic physics laboratories. The modulation range of u_l corresponds to varying R_p from near zero (pump beam blocked) to $R_{p,\max}$ (full pump power), with the operating point $R_{p,0}$ set to maintain the desired equilibrium polarization $P_{z,\text{eq}}$. Since the required control bandwidth is determined by $R_{\text{rel}} \approx 180\,\text{s}^{-1}$, the available pump modulation bandwidth far exceeds the control requirement.

Let $e_3 = [0, 0, 1]^\top$ and let $s_p \in (0, 1]$ denote the normalized photon spin along the pump direction. Define the pump photon spin vector as $\boldsymbol{S}_p = s_p e_3$. The total magnetic field is written as

$$\boldsymbol{B}(t) = \boldsymbol{B}_{\text{ext}}(t) + \boldsymbol{u}_m(t), \tag{12}$$

where $\boldsymbol{B}_{\text{ext}}(t)$ denotes the background magnetic field.

A continuous-time control-affine representation can be written as

$$\dot{\boldsymbol{P}} = \boldsymbol{f}\big(\boldsymbol{P}, t\big) + \sum_{i=1}^{4} \boldsymbol{g}_i(\boldsymbol{P})\, u_i = \boldsymbol{f}\big(\boldsymbol{P}, t\big) + \boldsymbol{G}(\boldsymbol{P})\, \boldsymbol{u}, \tag{13}$$

where the drift term is

$$\boldsymbol{f}(\boldsymbol{P}, t) = \frac{\gamma_e}{q}\, \boldsymbol{P} \times \boldsymbol{B}_{\text{ext}}(t) - \alpha\, \boldsymbol{P}, \qquad \alpha = \frac{R_{\text{rel}}}{q} > 0, \tag{14}$$

and the input vector fields are

$$\begin{aligned} \boldsymbol{g}_1(\boldsymbol{P}) &= \kappa_1 \begin{bmatrix} 0 \\ -P_z \\ P_y \end{bmatrix}, \quad \boldsymbol{g}_2(\boldsymbol{P}) = \kappa_1 \begin{bmatrix} P_z \\ 0 \\ -P_x \end{bmatrix}, \quad \boldsymbol{g}_3(\boldsymbol{P}) = \kappa_1 \begin{bmatrix} -P_y \\ P_x \\ 0 \end{bmatrix}, \\ \boldsymbol{g}_4(\boldsymbol{P}) &= \kappa_2 \begin{bmatrix} -P_x \\ -P_y \\ s_p - P_z \end{bmatrix} = \kappa_2 \big(\boldsymbol{S}_p - \boldsymbol{P}\big), \end{aligned} \tag{15}$$

with $\kappa_1 = \gamma_e / q > 0$ and $\kappa_2 = 1/q > 0$.

Accepted

https://www.sciengine.com/doi/10.1007/s11432-026-4965-x

For compactness, define

$$\boldsymbol{G}(\boldsymbol{P}) = \Big[\boldsymbol{G}_m(\boldsymbol{P})\ \boldsymbol{g}_4(\boldsymbol{P})\Big] \in \mathbb{R}^{3\times 4}, \qquad \boldsymbol{G}_m(\boldsymbol{P}) = \kappa_1 \begin{bmatrix} 0 & P_z & -P_y \\ -P_z & 0 & P_x \\ P_y & -P_x & 0 \end{bmatrix}. \tag{16}$$

The matrix $\boldsymbol{G}_m(\boldsymbol{P})$ is skew-symmetric and satisfies $\boldsymbol{G}_m(\boldsymbol{P})\,\boldsymbol{P} = \boldsymbol{0}$ for all $\boldsymbol{P}$.

4.2 Analysis of sub-actuation with magnetic fields only

Consider the standard configuration in which only the tri-axial magnetic field $\boldsymbol{u}_m$ is used for actuation and the pump channel is held constant. Under this configuration, the dynamics (13) reduce to

$$\dot{\boldsymbol{P}} = \boldsymbol{f}_{\text{std}}(\boldsymbol{P}, t) + \boldsymbol{B}_{\text{std}}(\boldsymbol{P})\,\boldsymbol{u}_m, \tag{17}$$

where $\boldsymbol{f}_{\text{std}}(\boldsymbol{P}, t)$ collects all terms independent of $\boldsymbol{u}_m$ and

$$\boldsymbol{B}_{\text{std}}(\boldsymbol{P}) = \frac{\gamma_e}{q} \begin{bmatrix} 0 & -P_z & P_y \\ P_z & 0 & -P_x \\ -P_y & P_x & 0 \end{bmatrix}. \tag{18}$$

Theorem 1. For any $\boldsymbol{P} \neq \boldsymbol{0}$, the magnetic input matrix $\boldsymbol{B}_{\text{std}}(\boldsymbol{P})$ in (17) is rank deficient and satisfies $\operatorname{rank}\big(\boldsymbol{B}_{\text{std}}(\boldsymbol{P})\big) = 2$. Moreover, the instantaneous control action $\boldsymbol{B}_{\text{std}}(\boldsymbol{P})\,\boldsymbol{u}_m$ is orthogonal to $\boldsymbol{P}$ for all $\boldsymbol{u}_m$. As a consequence, the system is instantaneously uncontrollable along the direction of $\boldsymbol{P}$ under magnetic actuation only.

Proof. Since $\boldsymbol{B}_{\text{std}}(\boldsymbol{P})$ is a 3×3 skew-symmetric matrix for every $\boldsymbol{P}$, its determinant is identically zero, which implies rank deficiency. For $\boldsymbol{P} \neq \boldsymbol{0}$, the mapping $\boldsymbol{u}_m \mapsto \boldsymbol{P} \times \boldsymbol{u}_m$ has a one-dimensional kernel given by $\operatorname{span}\{\boldsymbol{P}\}$ and hence has rank two. Therefore $\operatorname{rank}\big(\boldsymbol{B}_{\text{std}}(\boldsymbol{P})\big) = 2$ holds for all $\boldsymbol{P} \neq \boldsymbol{0}$.

For any $\boldsymbol{u}_m$, one has

$$\boldsymbol{P}^\top \boldsymbol{B}_{\text{std}}(\boldsymbol{P})\,\boldsymbol{u}_m = \frac{\gamma_e}{q}\,\boldsymbol{P}^\top\big(\boldsymbol{P} \times \boldsymbol{u}_m\big) = 0, \tag{19}$$

which proves that $\boldsymbol{B}_{\text{std}}(\boldsymbol{P})\,\boldsymbol{u}_m$ is always orthogonal to $\boldsymbol{P}$. This shows that the direction parallel to $\boldsymbol{P}$ cannot be actuated instantaneously by magnetic inputs alone.

Remark 2. The rank deficiency in (18) explains the limitation of standard magnetic feedback designs. Magnetic actuation can rotate the spin polarization direction but cannot directly generate a driving component along the instantaneous spin direction. Variations of the polarization magnitude are thus governed primarily by the relaxation and pumping processes rather than by direct magnetic control.

4.3 Model transformation: multiphysics augmentation

Now incorporate the pump channel u_l as an additional actuation input. The augmented input matrix is $\boldsymbol{G}(\boldsymbol{P}) \in \mathbb{R}^{3\times 4}$ defined in (16). The following lemma characterizes a verifiable full-row-rank condition.

Lemma 3. Let $\boldsymbol{P} \in \mathbb{R}^3$ and let $\boldsymbol{G}_m(\boldsymbol{P})$ be defined in (16). If $\boldsymbol{P} \neq \boldsymbol{0}$, then

$$\operatorname{rank}\big(\boldsymbol{G}_m(\boldsymbol{P})\big) = 2, \qquad \operatorname{Ker}\big(\boldsymbol{G}_m(\boldsymbol{P})\big) = \operatorname{span}\{\boldsymbol{P}\}, \qquad \operatorname{Im}\big(\boldsymbol{G}_m(\boldsymbol{P})\big) = \{v \in \mathbb{R}^3 :\ \boldsymbol{P}^\top v = 0\}. \tag{20}$$

Proof. From the identity $\boldsymbol{G}_m(\boldsymbol{P})\,\boldsymbol{B} = \kappa_1(\boldsymbol{P} \times \boldsymbol{B})$, one has $\boldsymbol{G}_m(\boldsymbol{P})\,\boldsymbol{P} = \boldsymbol{0}$ and hence $\operatorname{span}\{\boldsymbol{P}\} \subseteq \operatorname{Ker}(\boldsymbol{G}_m(\boldsymbol{P}))$. If $\boldsymbol{P} \neq \boldsymbol{0}$ and $\boldsymbol{P} \times \boldsymbol{B} = \boldsymbol{0}$, then $\boldsymbol{B}$ must be collinear with $\boldsymbol{P}$, which yields $\operatorname{Ker}(\boldsymbol{G}_m(\boldsymbol{P})) = \operatorname{span}\{\boldsymbol{P}\}$. Therefore $\operatorname{rank}(\boldsymbol{G}_m(\boldsymbol{P})) = 2$. Moreover, $\boldsymbol{P}^\top(\boldsymbol{P} \times \boldsymbol{B}) = 0$ for all $\boldsymbol{B}$ implies $\operatorname{Im}(\boldsymbol{G}_m(\boldsymbol{P})) \subseteq \{v : \boldsymbol{P}^\top v = 0\}$. Since both subspaces have dimension two, they coincide.

Lemma 4. Assume $\boldsymbol{P} \neq \boldsymbol{0}$. The augmented input matrix $\boldsymbol{G}(\boldsymbol{P})$ satisfies $\operatorname{rank}\big(\boldsymbol{G}(\boldsymbol{P})\big) = 3$ if and only if

$$\boldsymbol{P}^\top \boldsymbol{G}_4(\boldsymbol{P}) \neq 0 \quad \Longleftrightarrow \quad s_p P_z - \|\boldsymbol{P}\|^2 \neq 0. \tag{21}$$

Under (21), the SERF system (13) is fully actuated in the sense that $\boldsymbol{G}(\boldsymbol{P})$ has full row rank with input redundancy.

Accepted

https://www.sciengine.com/doi/10.1007/s11432-026-4965-x

Proof. By Lemma 3, $\mathrm{Im}\big(\boldsymbol{G}_m(\boldsymbol{P})\big) = \{v : \boldsymbol{P}^\top v = 0\}$. Therefore $\boldsymbol{G}(\boldsymbol{P})$ has rank three if and only if $\boldsymbol{G}_4(\boldsymbol{P})$ does not belong to $\mathrm{Im}\big(\boldsymbol{G}_m(\boldsymbol{P})\big)$, which is equivalent to $\boldsymbol{P}^\top \boldsymbol{G}_4(\boldsymbol{P}) \neq 0$. Using (15), one obtains

$$\boldsymbol{P}^\top \boldsymbol{G}_4(\boldsymbol{P}) = \kappa_2\, \boldsymbol{P}^\top \big(\boldsymbol{S}_p - \boldsymbol{P}\big) = \kappa_2 \big(s_p P_z - \|\boldsymbol{P}\|^2\big).$$

Since $\kappa_2 > 0$, condition (21) follows.

Remark 3. Condition (21) fails on the set $\{\boldsymbol{P} :\ \boldsymbol{P} = \boldsymbol{0} \text{ or } s_p P_z = \|\boldsymbol{P}\|^2\}$. This set has Lebesgue measure zero. Define the admissible domain as $\mathcal{D}_a = \{\boldsymbol{P} \in \mathbb{R}^3 :\ \boldsymbol{P} \neq \boldsymbol{0} \text{ and } s_p P_z \neq \|\boldsymbol{P}\|^2\}$. The singular set $\mathcal{S} = \mathbb{R}^3 \setminus \mathcal{D}_a$ has Lebesgue measure zero. In SERF operation, the polarization typically evolves in $\mathcal{D}_a$ that stays away from this set, and the full-row-rank property holds throughout that domain. In particular, the condition $s_p P_z = \|\boldsymbol{P}\|^2$ defines a sphere $P_x^2 + P_y^2 + (P_z - s_p/2)^2 = (s_p/2)^2$ of radius $s_p/2$ centred at $(0, 0, s_p/2)$. The pump laser maintains the polarization near $P_z \approx P_{z,0} \approx 0.5$ with $P_x, P_y \ll 1$, so that $\|\boldsymbol{P}\|^2 \approx P_z^2 \approx 0.25$ while $s_p P_z \approx 0.5$; the operating trajectory therefore stays well away from this singular sphere. Consequently, the operating trajectory remains well within $\mathcal{D}_a$ throughout normal operation.

4.4 Derivation of HOFA model

Having established the full-row-rank property of the augmented actuation in Section 4.3, we derive a second-order HOFA representation by treating the input rate as a virtual control. This representation is used to incorporate actuator rate constraints and to obtain the standard second-order form required by the parametric design framework in Section 5.

Differentiating (13) with respect to time yields

$$\ddot{\boldsymbol{P}} = \frac{d}{dt}\boldsymbol{f}(\boldsymbol{P}, t) + \frac{d}{dt}\big(\boldsymbol{G}(\boldsymbol{P})\,\boldsymbol{u}\big). \tag{22}$$

Applying the chain rule gives

$$\frac{d}{dt}\boldsymbol{f}(\boldsymbol{P}, t) = \frac{\partial \boldsymbol{f}}{\partial \boldsymbol{P}}\,\dot{\boldsymbol{P}} + \frac{\partial \boldsymbol{f}}{\partial t}, \tag{23}$$

and

$$\frac{d}{dt}\big(\boldsymbol{G}(\boldsymbol{P})\,\boldsymbol{u}\big) = \dot{\boldsymbol{G}}(\boldsymbol{P}, \dot{\boldsymbol{P}})\,\boldsymbol{u} + \boldsymbol{G}(\boldsymbol{P})\,\dot{\boldsymbol{u}}, \tag{24}$$

where $\dot{\boldsymbol{G}}(\boldsymbol{P}, \dot{\boldsymbol{P}})$ denotes the time derivative of $\boldsymbol{G}(\boldsymbol{P})$ along system trajectories.

Define the virtual input as the input rate

$$\boldsymbol{v} = \dot{\boldsymbol{u}} = \begin{bmatrix} \dot{\boldsymbol{u}}_m^\top & \dot{u}_l \end{bmatrix}^\top \in \mathbb{R}^4. \tag{25}$$

Substituting (23) and (24) into (22) yields the second-order HOFA form

$$\ddot{\boldsymbol{P}} = \boldsymbol{\chi}(\boldsymbol{P}, \dot{\boldsymbol{P}}, \boldsymbol{u}, t) + \boldsymbol{G}(\boldsymbol{P})\,\boldsymbol{v}, \tag{26}$$

where

$$\boldsymbol{\chi}(\boldsymbol{P}, \dot{\boldsymbol{P}}, \boldsymbol{u}, t) = \frac{\partial \boldsymbol{f}}{\partial \boldsymbol{P}}\,\dot{\boldsymbol{P}} + \frac{\partial \boldsymbol{f}}{\partial t} + \dot{\boldsymbol{G}}(\boldsymbol{P}, \dot{\boldsymbol{P}})\,\boldsymbol{u}. \tag{27}$$

Assumption 1. To obtain an explicit expression of $\boldsymbol{\chi}$, assume that the background magnetic field is slowly varying so that $\dot{\boldsymbol{B}}_{\mathrm{ext}}(t)$ is negligible over the control bandwidth. Under this assumption, $\partial \boldsymbol{f}/\partial t$ can be neglected.

This assumption is well justified in the primary application scenario of SERF atomic magnetometers operating inside multi-layer magnetic shielding. In a typical shielded environment, the residual magnetic field B_{ext} is on the order of 1 nT and varies on time scales of seconds to minutes, whereas the spin dynamics evolve on a time scale of $1/R_{\mathrm{rel}} \approx 5.6$ ms. The ratio of the field variation rate to the spin relaxation rate is therefore $\|\dot{\boldsymbol{B}}_{\mathrm{ext}}\|/(R_{\mathrm{rel}}\|\boldsymbol{B}_{\mathrm{ext}}\|) \ll 1$, making the $\partial \boldsymbol{f}/\partial t$ term negligible over the control bandwidth. In unshielded or weakly shielded scenarios where the background field varies rapidly, the term $\partial \boldsymbol{f}/\partial t$ should be retained or estimated online. Using (14) and the identity $\frac{d}{dt}(\boldsymbol{P} \times \boldsymbol{B}) = \dot{\boldsymbol{P}} \times \boldsymbol{B} + \boldsymbol{P} \times \dot{\boldsymbol{B}}$, one obtains

$$\boldsymbol{\chi}(\boldsymbol{P}, \dot{\boldsymbol{P}}, \boldsymbol{u}, t) = \frac{1}{q}\Big[\gamma_e\, \dot{\boldsymbol{P}} \times \big(\boldsymbol{B}_{\mathrm{ext}} + \boldsymbol{u}_m\big) - \big(R_{\mathrm{rel}} + u_l\big)\dot{\boldsymbol{P}}\Big]. \tag{28}$$

Remark 4. Equation (26) is a second-order input rate model with full actuation. On the admissible operating domain specified in Remark 3, the matrix $\boldsymbol{G}(\boldsymbol{P})$ has full row rank and the virtual input $\boldsymbol{v}$ can be used to cancel $\boldsymbol{\chi}$ and assign a desired constant linear error dynamics in subsequent controller design.

Accepted

https://www.sciengine.com/doi/10.1007/s11432-026-4965-x

5 Controller design

Based on the HOFA model (26), this section presents a decoupling tracking controller under full actuation. We first construct a parametric virtual control law and establish asymptotic tracking via Lyapunov analysis. We then clarify the decoupling mechanism and provide a principled parameter configuration.

5.1 Parametric design and stability analysis

Let the desired reference trajectory be $\boldsymbol{P}_d(t) \in \mathbb{R}^3$ with bounded $\dot{\boldsymbol{P}}_d(t)$ and $\ddot{\boldsymbol{P}}_d(t)$. Define the tracking error

$$\boldsymbol{e}(t) = \boldsymbol{P}(t) - \boldsymbol{P}_d(t), \tag{29}$$

and define the desired second-order error dynamics

$$\ddot{\boldsymbol{e}}(t) + \boldsymbol{K}_D\dot{\boldsymbol{e}}(t) + \boldsymbol{K}_P\boldsymbol{e}(t) = \boldsymbol{0}, \tag{30}$$

where $\boldsymbol{K}_P, \boldsymbol{K}_D \in \mathbb{R}^{3\times 3}$ are constant design matrices.

Let the requested acceleration command be

$$\boldsymbol{v}_{\text{req}}(t) = \ddot{\boldsymbol{P}}_d(t) - \boldsymbol{K}_D\dot{\boldsymbol{e}}(t) - \boldsymbol{K}_P\boldsymbol{e}(t). \tag{31}$$

Theorem 2. Consider the SERF system in the second-order HOFA form (26). Assume that $\boldsymbol{P}(t)$ evolves in the admissible domain $\mathcal{D}_a$ defined in Remark 3, on which $\boldsymbol{G}(\boldsymbol{P})$ has full row rank. Let $\boldsymbol{G}^{\dagger}(\boldsymbol{P}) \in \mathbb{R}^{4\times 3}$ be any right inverse satisfying

$$\boldsymbol{G}(\boldsymbol{P})\,\boldsymbol{G}^{\dagger}(\boldsymbol{P}) = I_3. \tag{32}$$

Choose $\boldsymbol{K}_P$ and $\boldsymbol{K}_D$ such that the matrix polynomial $D(s) = s^2 I_3 + s\boldsymbol{K}_D + \boldsymbol{K}_P$ is Hurwitz. Then the virtual control law

$$\boldsymbol{v} = \boldsymbol{G}^{\dagger}(\boldsymbol{P})\Big(\boldsymbol{v}_{\text{req}} - \boldsymbol{\chi}(\boldsymbol{P}, \dot{\boldsymbol{P}}, \boldsymbol{u}, t)\Big) + \Big(I_4 - \boldsymbol{G}^{\dagger}(\boldsymbol{P})\,\boldsymbol{G}(\boldsymbol{P})\Big)\boldsymbol{z}, \tag{33}$$

with an arbitrary $\boldsymbol{z}(t) \in \mathbb{R}^4$, yields $\lim_{t\to\infty} \boldsymbol{e}(t) = \boldsymbol{0}$ and $\lim_{t\to\infty} \dot{\boldsymbol{e}}(t) = \boldsymbol{0}$.

Proof. Substituting (33) into (26) gives

$$\ddot{\boldsymbol{P}} = \boldsymbol{\chi}(\boldsymbol{P}, \dot{\boldsymbol{P}}, \boldsymbol{u}, t) + \boldsymbol{G}(\boldsymbol{P})\,\boldsymbol{G}^{\dagger}(\boldsymbol{P})\Big(\boldsymbol{v}_{\text{req}} - \boldsymbol{\chi}(\boldsymbol{P}, \dot{\boldsymbol{P}}, \boldsymbol{u}, t)\Big) + \boldsymbol{G}(\boldsymbol{P})\Big(I_4 - \boldsymbol{G}^{\dagger}(\boldsymbol{P})\,\boldsymbol{G}(\boldsymbol{P})\Big)\boldsymbol{z}.$$

Using (32) and $\boldsymbol{G}(\boldsymbol{P})\big(I_4 - \boldsymbol{G}^{\dagger}(\boldsymbol{P})\boldsymbol{G}(\boldsymbol{P})\big) = \boldsymbol{0}$, one obtains

$$\ddot{\boldsymbol{P}} = \boldsymbol{v}_{\text{req}}. \tag{34}$$

Combining (34) with the identity $\ddot{\boldsymbol{e}} = \ddot{\boldsymbol{P}} - \ddot{\boldsymbol{P}}_d$ yields the error dynamics (30).

Define the augmented error state $\boldsymbol{\xi} = [\boldsymbol{e}^{\top}, \dot{\boldsymbol{e}}^{\top}]^{\top} \in \mathbb{R}^6$, which satisfies

$$\dot{\boldsymbol{\xi}} = A_{\text{cl}}\boldsymbol{\xi}, \qquad A_{\text{cl}} = \begin{bmatrix} \boldsymbol{0}_{3\times 3} & I_3 \\ -\boldsymbol{K}_P & -\boldsymbol{K}_D \end{bmatrix}. \tag{35}$$

Since $D(s)$ is Hurwitz, A_{cl} is Hurwitz. For any $Q = Q^{\top} \succ 0$, there exists a unique $P = P^{\top} \succ 0$ solving

$$A_{\text{cl}}^{\top}P + PA_{\text{cl}} = -Q. \tag{36}$$

Let $V(\boldsymbol{\xi}) = \boldsymbol{\xi}^{\top}P\boldsymbol{\xi}$. Along trajectories of (35),

$$\dot{V}(\boldsymbol{\xi}) = \boldsymbol{\xi}^{\top}(A_{\text{cl}}^{\top}P + PA_{\text{cl}})\boldsymbol{\xi} = -\boldsymbol{\xi}^{\top}Q\boldsymbol{\xi},$$

which is negative definite for all $\boldsymbol{\xi} \neq \boldsymbol{0}$. Therefore $\boldsymbol{\xi}(t) \to \boldsymbol{0}$ and hence $\boldsymbol{e}(t) \to \boldsymbol{0}$ and $\dot{\boldsymbol{e}}(t) \to \boldsymbol{0}$.

Remark 5. The term $\big(I_4 - \boldsymbol{G}^{\dagger}(\boldsymbol{P})\boldsymbol{G}(\boldsymbol{P})\big)\boldsymbol{z}$ belongs to the null space of $\boldsymbol{G}(\boldsymbol{P})$ and does not affect the error dynamics. It can be used to incorporate secondary objectives such as input energy shaping, rate limiting, or operating-point regulation under redundancy.

Remark 6. In numerical implementation, $\boldsymbol{G}^{\dagger}(\boldsymbol{P})$ can be chosen as a damped right inverse to improve robustness near ill-conditioned operating points. This implementation choice does not change the structural cancellation argument as long as $\boldsymbol{G}(\boldsymbol{P})\boldsymbol{G}^{\dagger}(\boldsymbol{P})$ remains sufficiently close to I_3 over the operating domain.

Accepted

https://www.sciengine.com/doi/10.1007/s11432-026-4965-x

Remark 7. In practical implementation, the physical inputs $\boldsymbol{u}$ are subject to amplitude and rate constraints. The amplitude of $\boldsymbol{u}_m$ is limited by the coil driver range and u_l is bounded by the achievable optical pumping rate. Since the HOFA model is formulated in terms of input rates, the virtual control $\boldsymbol{v}$ directly represents $\dot{\boldsymbol{u}}$, and rate saturation can be enforced by clipping $\boldsymbol{v}$ prior to integration without altering the decoupling structure. Furthermore, the null-space term $(I_4 - \boldsymbol{G}^{\dagger}\boldsymbol{G})\boldsymbol{z}$ in the allocation law (33) provides additional freedom to optimize actuator usage under amplitude constraints. For the SERF platform considered herein, the actuator bandwidths (magnetic coils $> 1\,\mathrm{kHz}$, pump laser modulation $> 100\,\mathrm{kHz}$) substantially exceed the control bandwidth dictated by the spin relaxation rate R_{rel}, so saturation is not expected under nominal operating conditions.

5.2 Decoupling mechanism and parameter configuration

The SERF spin dynamics exhibit strong cross-axis coupling due to the vector-product interaction and the state dependent actuation directions. Under the virtual-input design (33), the coupling is removed at the level of the closed loop error dynamics (30), which becomes a constant linear differential equation.

5.2.1 *Mathematical decoupling under diagonal gains*

Proposition 1. Consider the closed loop system induced by (33). If the gain matrices are chosen as

$$\boldsymbol{K}_P = \mathrm{diag}\{k_{p1}, k_{p2}, k_{p3}\}, \qquad \boldsymbol{K}_D = \mathrm{diag}\{k_{d1}, k_{d2}, k_{d3}\}, \tag{37}$$

then the error dynamics (30) decouple into three independent scalar second-order equations. In particular, for each $i \in \{x, y, z\}$,

$$\ddot{e}_i(t) + k_{di}\dot{e}_i(t) + k_{pi}e_i(t) = 0. \tag{38}$$

Proof. Substituting (37) into (30) yields a diagonal linear operator on $\boldsymbol{e}$. Therefore the vector equation decomposes into the three scalar equations (38).

5.2.2 *Actuator coordination under redundancy*

The diagonal choice (37) guarantees decoupling at the virtual-dynamics level. The mapping from the virtual input $\boldsymbol{v}$ to the physical input rate is realized through the right-inverse allocation in (33). The magnetic channels $\boldsymbol{u}_m$ generate instantaneous motions orthogonal to $\boldsymbol{P}$, while the pump channel u_l contributes a component that is not restricted to the orthogonal complement of $\boldsymbol{P}$. The redundancy enables the allocator to synthesize the requested acceleration $\boldsymbol{v}_{\mathrm{req}}$ without cross-axis coupling in the closed loop error dynamics.

6 Simulation results

This section evaluates the proposed HOFA based controller against a baseline control strategy designed for an under actuated system (UAS), abbreviated as UAS control, under three scenarios. The scenarios include decoupling validation under a smooth staircase command, three axis stochastic trajectory tracking, and disturbance rejection under multiple perturbation levels. All simulations use the same SERF spin polarization plant (13) and its HOFA form (26), the same discretization scheme, and identical initial conditions and reference or disturbance profiles.

The state is the spin polarization $\boldsymbol{P}(t) = [P_x(t), P_y(t), P_z(t)]^{\top} \in \mathbb{R}^3$. The multiphysics input is $\boldsymbol{u}(t) = [\boldsymbol{u}_m^{\top}(t)\ u_l(t)]^{\top} \in \mathbb{R}^4$, where $\boldsymbol{u}_m(t) = [B_x(t), B_y(t), B_z(t)]^{\top}$ denotes the triaxial magnetic fields and $u_l(t)$ denotes the pump laser actuation channel. The normalized photon spin is $\boldsymbol{S}_p = s_p e_3$ with $e_3 = [0, 0, 1]^{\top}$.

The continuous-time plant (13) is simulated using forward Euler with sampling period $T_s = 10^{-5}\,\mathrm{s}$,

$$\boldsymbol{P}_{k+1} = \boldsymbol{P}_k + T_s\,\dot{\boldsymbol{P}}(\boldsymbol{P}_k, \boldsymbol{u}_k)\,. \tag{39}$$

Consistent with the HOFA construction, the virtual input is defined as $\boldsymbol{v}(t) = \dot{\boldsymbol{u}}(t)$ and the physical input is updated by

$$\boldsymbol{u}_{k+1} = \boldsymbol{u}_k + T_s\,\boldsymbol{v}_k. \tag{40}$$

In implementation, a damped right inverse is used for numerical robustness,

$$\boldsymbol{G}_{\varepsilon}^{\dagger}(\boldsymbol{P}) = \boldsymbol{G}^{\top}(\boldsymbol{P})\Big(\boldsymbol{G}(\boldsymbol{P})\boldsymbol{G}^{\top}(\boldsymbol{P}) + \varepsilon I_3\Big)^{-1}, \qquad \varepsilon = 10^{-9}. \tag{41}$$

Accepted

https://www.sciengine.com/doi/10.1007/s11432-026-4965-x

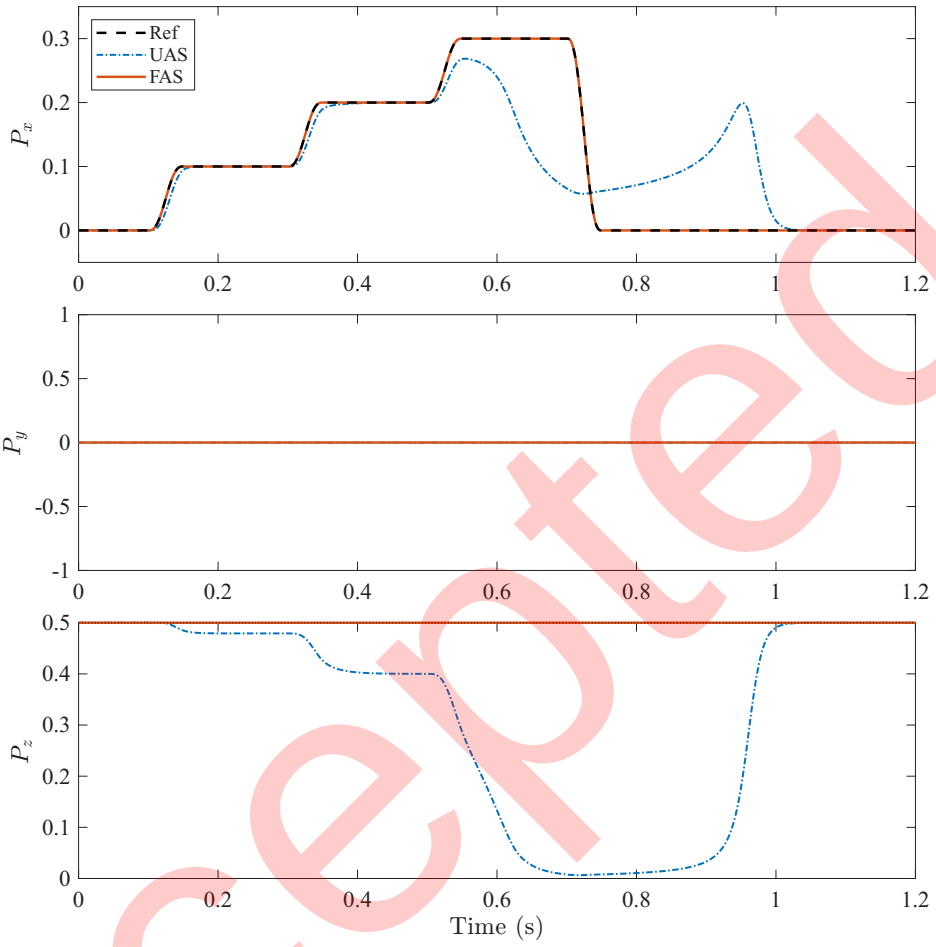


Figure 2 Decoupling validation under a smooth staircase command on P_x: reference and responses of the FAS method and the UAS baseline.

The simulations adopt $q = 4$, $R_{\text{rel}} = 180$, and $s_p = 1$. The baseline pump level $u_{l,0}$ is selected such that the equilibrium satisfies $\boldsymbol{u}_m = \mathbf{0}$ and $P_z = 0.5$, which is consistent with the operating point setting used throughout the paper. Unless otherwise stated, the null-space term in (33) is disabled by setting $\boldsymbol{z}(t) \equiv \mathbf{0}$.

Define the tracking error by (29). The proposed controller uses the cancellation and assignment structure (33) with diagonal $\boldsymbol{K}_P$ and $\boldsymbol{K}_D$, which yields the decoupled error dynamics (30). The UAS baseline adopts the standard magnetic only actuation configuration by fixing $u_l(t) \equiv u_{l,0}$ and generating $\boldsymbol{u}_m(t)$ through independent single-axis linear feedback with integral action. This baseline reflects the practical constraint of under actuated magnetic control and serves as a reference for assessing the benefit of full actuation and HOFA based allocation.

The gains of both controllers are tuned to provide comparable closed loop performance so that the comparison isolates the structural benefit of full actuation. For the proposed FAS controller, the diagonal gains $\boldsymbol{K}_D = 240\, I_3$ and $\boldsymbol{K}_P = 22500\, I_3$ place the closed loop poles of the decoupled error dynamics at $s = -120 \pm j\,90$ (natural frequency $\omega_n = 150\,\text{rad/s}$, damping ratio $\zeta = 0.8$). For the UAS baseline, the PI gains $(k_p, k_i) = (5,\, 455)$ yield a linearized natural frequency $\sqrt{K \cdot k_i} \approx 100\,\text{rad/s}$, where $K = \gamma_e P_{z,0}$ is the linearized input gain, thereby keeping the UAS baseline in the same bandwidth order as the FAS controller while preserving its magnetic only actuation structure. The moderately lower UAS bandwidth makes the comparison conservative: any performance advantage of the FAS controller cannot be attributed to bandwidth mismatch.

6.1 Decoupling validation under smooth staircase command

This experiment validates decoupling by exciting only the x axis reference while holding the other axes constant. The reference $P_{x,d}(t)$ is generated by superimposing four C^2-continuous smooth steps at $t = \{0.1,\, 0.3,\, 0.5,\, 0.7\}\,\text{s}$ with amplitudes $\Delta = \{+0.1,\, +0.1,\, +0.1,\, -0.3\}$ and a common transition duration $T_{\text{rise}} = 0.05\,\text{s}$. The other references are fixed as $P_{y,d}(t) \equiv 0$ and $P_{z,d}(t) \equiv 0.5$. The simulation horizon is $T_{\text{end}} = 1.2\,\text{s}$.

For the proposed method, the diagonal gains are chosen as $\boldsymbol{K}_D = 240\, I_3$ and $\boldsymbol{K}_P = 22500\, I_3$. For the UAS

https://www.sciengine.com/doi/10.1007/s11432-026-4965-x

Accepted

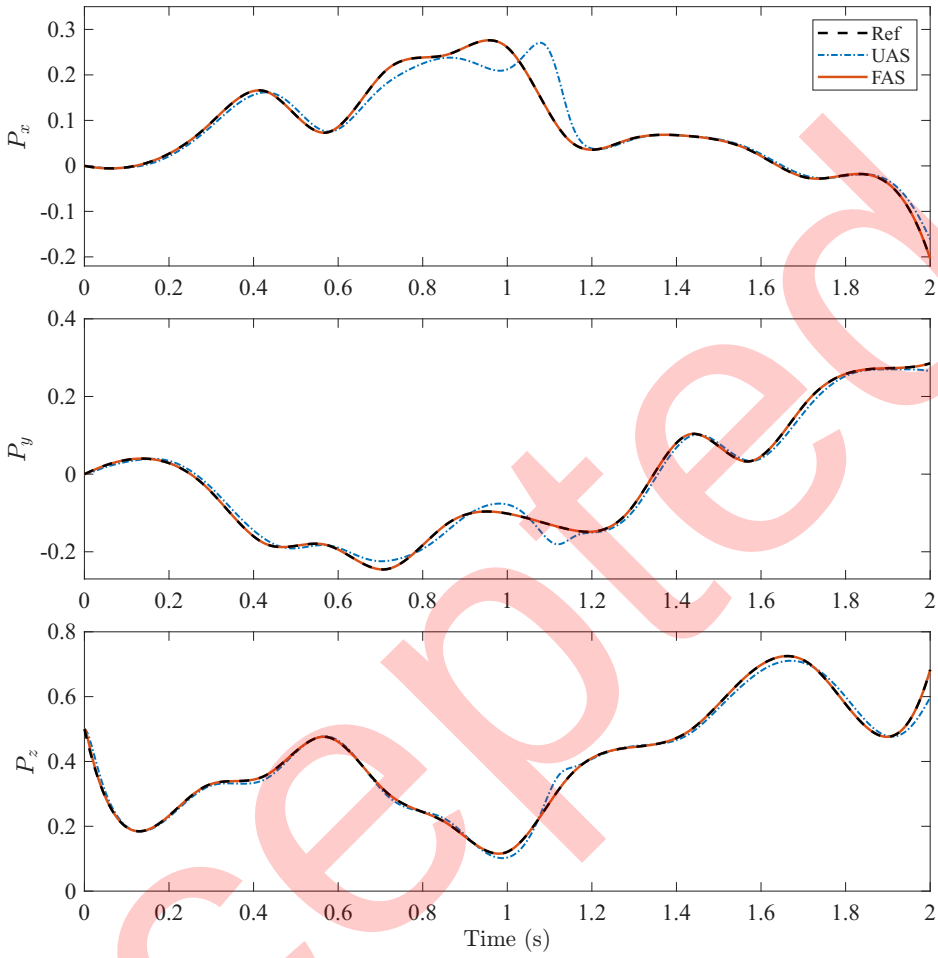


Figure 3 Three-axis stochastic trajectory tracking with first-order autoregressive references: reference and responses of the FAS method and the UAS baseline.

baseline, the magnetic loop gains are selected as $(k_p, k_i) = (5, 455)$ for the x axis regulation under the same reference profile.

Figure 2 shows that the proposed controller tracks P_x over a wide range while maintaining negligible inter-axis deviations. The responses on P_y remain close to zero and the longitudinal component P_z stays regulated around 0.5. Under the UAS baseline, the P_x tracking range is reduced and the response induces visible variations in P_z, which is consistent with the rank-deficient magnetic actuation that cannot directly enforce independent regulation along the spin polarization direction.

Table 1 Quantitative performance metrics for the staircase decoupling test.

Metric	FAS (Proposed)	UAS (Baseline)
RMSE(P_x)	7.4×10^{-6}	7.8×10^{-2}
RMSE(P_z) (cross-axis)	2.1×10^{-6}	2.7×10^{-1}

6.2 Three-axis stochastic trajectory tracking with first-order autoregressive references

This experiment evaluates large amplitude tracking by commanding all three axes to follow independent stochastic references. Each axis reference is generated by a first-order autoregressive process sampled every $\Delta t_{\mathrm{ar}} = 0.15\,\mathrm{s}$,

$$p_k = \phi p_{k-1} + \sigma \epsilon_k, \qquad \epsilon_k \sim \mathcal{N}(0, 1), \tag{42}$$

with $(\phi, \sigma) = (0.85,\ 0.1)$. A fixed random seed 101 is used for reproducibility. The sampled points are interpolated using cubic splines to obtain $\boldsymbol{P}_d(t)$ and its derivatives $\dot{\boldsymbol{P}}_d(t)$ and $\ddot{\boldsymbol{P}}_d(t)$ required by (31). The reference is constrained

Accepted
https://www.sciengine.com/doi/10.1007/s11432-026-4965-x

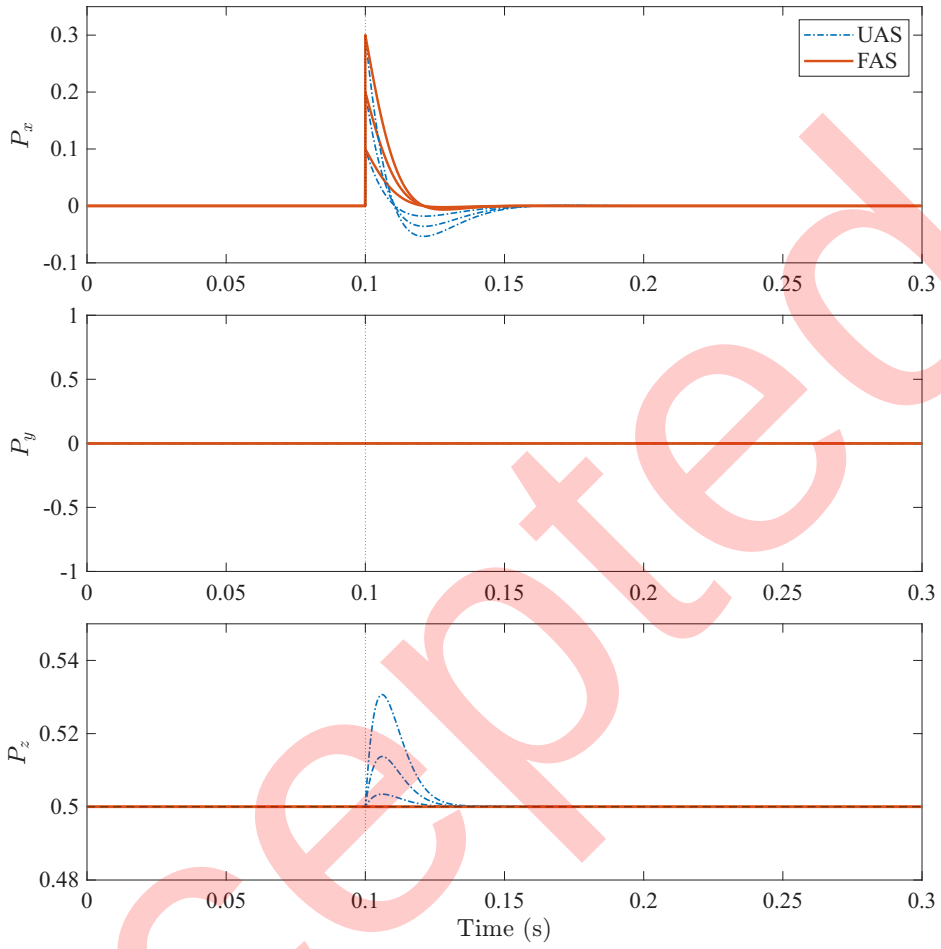


Figure 4 Disturbance rejection under multiple injected disturbances Δ on P_x: responses of the FAS method and the UAS baseline.

to a physically meaningful domain by enforcing $P_x, P_y \in [-0.4, 0.4]$ and $P_z \in [0.1, 0.9]$ with P_z centered at 0.5. The simulation horizon is $T_{\text{end}} = 2.0\,\text{s}$.

For the proposed method, the diagonal gains are chosen as $\boldsymbol{K}_D = 240\, I_3$ and $\boldsymbol{K}_P = 22500\, I_3$. For the UAS baseline, the pump input is held at $u_l(t) \equiv u_{l,0}$ and the transverse magnetic loop gains are set as $(k_{p,xy}, k_{i,xy}) = (5,\, 455)$.

Figure 3 shows that the proposed method yields clean tracking responses on all axes with limited inter-axis interaction, which is consistent with the decoupled error dynamics (30). The UAS baseline exhibits noticeable inter-axis interactions during rapid reference variations, and the longitudinal component deviates in a manner that reflects the lack of direct actuation authority along the spin polarization direction under magnetic only control.

Table 2 Quantitative performance metrics for the three-axis AR(1) tracking test.

Metric	FAS (Proposed)	UAS (Baseline)
RMSE(P_x)	3.4×10^{-5}	2.9×10^{-2}
RMSE(P_y)	1.0×10^{-4}	1.3×10^{-2}
RMSE(P_z)	1.1×10^{-3}	1.5×10^{-2}

6.3 Disturbance rejection under multiple perturbation levels

This experiment evaluates disturbance rejection by injecting an impulsive perturbation on the x axis at $T_d = 0.1\,\text{s}$. The reference is held constant at $\boldsymbol{P}_d(t) \equiv [0,\, 0,\, 0.5]^\top$. The perturbation is applied by

$$P_x(T_d^+) = P_x(T_d^-) + \Delta, \tag{43}$$

Accepted

https://www.sciengine.com/doi/10.1007/s11432-026-4965-x

and Δ is swept over $\{0.1, 0.2, 0.3\}$ to form a family of response curves. The simulation horizon is $T_{\text{end}} = 0.3\,\text{s}$.

For the proposed method, the diagonal gains are chosen as $\boldsymbol{K}_D = 240\,I_3$ and $\boldsymbol{K}_P = 22500\,I_3$. For the UAS baseline, the pump input is fixed at $u_l(t) \equiv u_{l,0}$ and the magnetic loop gains are set as $(k_p, k_i) = (5, 455)$ for the disturbance rejection test.

Figure 4 shows that the proposed method restores P_x rapidly with limited rebound and maintains regulation of P_z without noticeable disturbance transmission. Here, rebound refers to the opposite-side excursion of P_x during post-disturbance recovery. The UAS baseline exhibits larger rebound and a visible deviation in P_z, which indicates that disturbances injected into the transverse component propagate through the coupled dynamics when actuation remains under actuated.

Table 3 Quantitative performance metrics for the disturbance rejection test with $\Delta = 0.2$.

Metric	FAS (Proposed)	UAS (Baseline)
Rebound(P_x)	2.2%	17.9%
$T_{2\%}(P_x)$	31 ms	50 ms
$e_{\max}(P_z)$ (cross-axis)	5.0×10^{-6}	1.4×10^{-2}

6.4 Discussion

Across all three simulation results, the proposed HOFA based controller achieves wide-range tracking and fast disturbance recovery without inter-axis coupling while maintaining regulation of P_z. These results support the decoupling claim established by the diagonal-gain design in (37) and the redundancy resolving allocation in (33). The comparison with the UAS baseline further illustrates that full actuation is essential for achieving independent three-axis regulation when the magnetic input mapping is structurally rank-deficient.

Tables 1, 2, and 3 report the quantitative comparison in a subsection-by-subsection manner. In the staircase test, Table 1 shows that the proposed method achieves an on-axis RMSE of 7.4×10^{-6} and a cross-axis P_z RMSE of 2.1×10^{-6}, whereas the UAS baseline yields errors that are two orders of magnitude larger. In the AR(1) tracking test, Table 2 shows that all three RMSE values remain below 1.1×10^{-3} for the proposed method but stay above 10^{-2} for the baseline. In the disturbance rejection test, Table 3 shows that the proposed method limits rebound to 2.2%, achieves a 2% settling time of 31 ms, and keeps the cross-axis P_z deviation at 5.0×10^{-6}, while the baseline exhibits 17.9% rebound, a 50 ms settling time, and a cross-axis deviation of 1.4×10^{-2}. These improvements are attributed to the decoupling structure enabled by full actuation and the right-inverse allocation, which eliminates the inter-axis coupling inherent in the under actuated magnetic only control scheme.

7 Conclusion

A FAS perspective is established for SERF magnetometer quantum spin dynamics governed by Bloch equations, and the algebraic singularity of standard magnetic actuation is characterized as a structural rank deficiency that prevents independent three-axis regulation. A multiphysics reconstruction is then developed by incorporating pump laser intensity as an active input, which yields an augmented input mapping that achieves full row rank on an admissible operating domain and thereby forms a fully actuated model. By treating the input rate as a virtual control, a HOFA representation is derived to support synthesis in the canonical fully actuated form.

Based on this representation, an explicit analytic controller is constructed by exact cancellation and parametric eigenstructure assignment, while a right-inverse allocation resolves actuation redundancy without altering the closed loop error dynamics. Under diagonal gain selection, the closed loop tracking error dynamics become a constant decoupled second-order linear system, which guarantees asymptotic tracking and complete dynamic decoupling. Numerical simulations validate the theoretical claims under smooth staircase excitation, three-axis stochastic trajectory tracking, and impulsive disturbance injection, showing wide-range tracking, limited inter-axis coupling, and fast recovery while maintaining longitudinal regulation.

Future work focuses on experimental validation on SERF platforms, robustness enhancement against parameter mismatch and unmodeled background-field variations, and constraint-aware allocation that explicitly accounts for actuator saturation and rate limits while preserving the fully actuated decoupling structure.

Acknowledgements This work is supported by the Natural Science Foundation of Zhejiang Province under Grant LQN26F030046; the National Natural Science Foundation of China under Grant 62505304; the National Natural Science Foundation of China under Grants 62525303 and 62576114; the National Natural Science Foundation of China under Grant 61673041; the National Science Foundation for Distinguished

Accepted
https://www.sciengine.com/doi/10.1007/s11432-026-4965-x

Young Scholars of China under Grant 62403173 and the Key Area Research and Development Program of Guangdong Province under Grant 2021B0101410005.

References

1 Huang X, Wang W, Hu Y, et al. Double spin resonance for traceable ultrasensitive atomic spin sensor. Physical Review Letters, 2025, 135: 043001
2 Wei K, Xu Z, He Y, et al. Dark matter search with a resonantly-coupled hybrid spin system. Reports on Progress in Physics, 2025, 88: 057801
3 Bloch I M, Shaham R, Hochberg Y, et al. Constraints on axion-like dark matter from a SERF comagnetometer. Nature Communications, 2023, 14: 5784
4 Kornack T W, Ghosh R K, Romalis M V. Nuclear spin gyroscope based on an atomic comagnetometer. Physical Review Letters, 2005, 95: 230801
5 Budker D, Romalis M. Optical magnetometry. Nature Physics, 2007, 3: 227–234
6 Sheng D, Li S, Dural N, et al. Subfemtotesla scalar atomic magnetometry using multipass cells. Physical Review Letters, 2013, 110: 160802
7 Qin J, Zhou Y, Wang Y. A high dynamic range and ultralow-noise bipolar current source for unshielded SERF atomic magnetometers. IEEE Transactions on Instrumentation and Measurement, 2021, 71: 1–8
8 Wang R, Wang Z, Liu S, et al. Optimal spin polarization control for the spin-exchange relaxation-free system using adaptive dynamic programming. IEEE Transactions on Neural Networks and Learning Systems, 2022, 35: 5835–5847
9 Pang H, Wang H, Zhang K, et al. High-precision in situ control of transverse magnetic field in ASGs based on high-frequency modulation and transient response. IEEE/ASME Transactions on Mechatronics, 2025, pages 1–12
10 Yan Y, Zhang S, Liu Z, et al. Optical parameter decoupling and optimization for elliptically polarized atomic magnetometer. IEEE Transactions on Instrumentation and Measurement, 2023, 73: 1–10
11 Li F, Wang Z, Wang R, et al. Magnetic field compensation control for spin-exchange relaxation-free comagnetometer using reinforcement learning. IEEE Transactions on Instrumentation and Measurement, 2023, 72: 1–10
12 Fan S, Pei H, Quan W, et al. Magnetic and optical control in thermal atomic spin ensembles: Principles and applications. Science China Physics, Mechanics & Astronomy, 2025, 68: 100301
13 Qin B, Wang Z, Wang R, et al. Modeling of nonlinear and nonstationary stochasticity for atomic ensembles. ISA Transactions, 2023, 143: 557–571
14 Qin B, Wang Z, Fan W, et al. A novel data-driven physical iterative modeling approach and its application in quantum instrumentation. IEEE Transactions on Systems, Man, and Cybernetics: Systems, 2024, 54: 5667–5679
15 Wang Z, Huang J, Quan W, et al. A data-driven state observation method for atomic spin-exchange relaxation-free comagnetometer. In: Proceedings of IEEE 8th Data Driven Control and Learning Systems Conference. IEEE, 2019. 876–882
16 Wang Z, Liu S, Wang R, et al. Atomic spin polarization controllability analysis: A novel controllability determination method for spin-exchange relaxation-free co-magnetometers. IEEE/CAA Journal of Automatica Sinica, 2021, 9: 699–708
17 Wang R, Wang Z, Ma C, et al. Reachability analysis of the atomic spin polarization for spin-exchange relaxation-free atomic magnetometers. In: Proceedings of International Conference on Control and Robotics. IEEE, 2022. 199–203
18 Duan G R. Fully actuated system approach for control: An overview. IEEE Transactions on Cybernetics, 2024, 54: 7285–7306
19 Duan G R. High-order fully actuated system approaches: Part I. models and basic procedure. International Journal of Systems Science, 2021, 52: 422–435
20 Duan G R. High-order fully actuated system approaches: Part II. generalized strict-feedback systems. International Journal of Systems Science, 2021, 52: 437–454
21 Duan G R. High-order fully actuated system approaches: Part III. robust control and high-order backstepping. International Journal of Systems Science, 2021, 52: 952–971
22 Duan G R. High-order fully actuated system approaches: Part IV. adaptive control and high-order backstepping. International Journal of Systems Science, 2021, 52: 972–989
23 Duan G R. High-order fully actuated system approaches: Part V. robust adaptive control. International Journal of Systems Science, 2021, 52: 2129–2143
24 Duan G R. High-order fully actuated system approaches: Part VII. controllability, stabilisability and parametric designs. International Journal of Systems Science, 2021, 52: 3091–3114
25 Zhao T, Duan G R. Fully actuated system approach to attitude control of flexible spacecraft with nonlinear time-varying inertia. Science China Information Sciences, 2022, 65: 212201
26 Duan G R. A FAS approach for stabilization of generalized chained systems: multi-vector case. Science China Information Sciences, 2025, 68: 162201
27 Qiu Y, Li Q. Event-triggered tracking control for a class of nonlinear systems based on high-order fully actuated system theory. Science China Information Sciences, 2025, 68: 159201
28 Wang C, Wang Z, Li W, et al. Composite disturbance filtering and full actuation control for fully observed systems. Science China Information Sciences, 2025, 68: 172202
29 Yao F, Tian G, Wu A, et al. A high-order fully actuated system approach to control of overhead cranes. IEEE/ASME Transactions on Mechatronics, 2025, 30: 2485–2496
30 Duan G R, Liu L, Liu H. Fully actuated system approach-based control design for three benchmark nonlinear underactuated systems. Control Engineering Practice, 2026, 168: 106728
31 Lin Z, Feng S, Zhang J, et al. Angular-velocity-free prescribed performance attitude control for spacecrafts based on high-order fully actuated system approach. Control Engineering Practice, 2026, 167: 106651
32 Duan G R, Hu L, Zhang S, et al. Substabilization for coupled-inverted pendulums with input failure: a fully actuated system approach. Science China Information Sciences, 2026, 69: 142201
33 Duan G R. Substability and substabilization: Control of subfully actuated systems. IEEE Transactions on Cybernetics, 2023, 53: 7309–7322

Accepted

https://www.sciengine.com/doi/10.1007/s11432-026-4965-x